The Meteoritical Society

Meteoritics & Planetary Science 50, Nr 8, 1423–1435 (2015)
doi: 10.1111/maps.12478

A novel approach to fireball modeling: The observable and the calculated

Eleanor Kate SANSOM[1*], Philip BLAND[1], Jonathan PAXMAN[2], and Martin TOWNER[1]

[1]Department of Applied Geology, Curtin University, GPO Box U1987, Perth, Western Australia 6845, Australia
[2]Department of Mechanical Engineering, Curtin University, GPO Box U1987, Perth, Western Australia 6845, Australia
[*]Corresponding author. E-mail: eleanor.sansom@postgrad.curtin.edu.au

(Received 16 September 2014; revision accepted 14 May 2015)

Abstract–Estimating the mass of a meteoroid passing through the Earth's atmosphere is essential to determining potential meteorite fall positions. High-resolution fireball images from dedicated camera networks provide the position and timing for fireball bright flight trajectories. There are two established mass determination methods: the photometric and the dynamic. A new approach is proposed, based on the dynamic method. A dynamic optimization initially constrains unknown meteoroid characteristics which are then used in a parametric model for an extended Kalman filter. The extended Kalman filter estimates the position, velocity, and mass of the meteoroid body throughout its flight, and quantitatively models uncertainties. Uncertainties have not previously been modeled so explicitly and are essential for determining fall distributions for potential meteorites. This two-step method aims to automate the process of mass determination for application to any trajectory data set and has been applied to observations of the Bunburra Rockhole fireball. The new method naturally handles noisy raw data. Initial and terminal bright flight mass results are consistent with other works based on the established photometric method and cosmic ray analysis. A full analysis of fragmentation and the variability in the heat-transfer coefficient will be explored in future versions of the model.

INTRODUCTION

The full potential of meteorite analysis for providing valuable insights about protoplanetary disk formation cannot be reached without first constraining their origins in the solar system. As with terrestrial rocks, without context (outcrop) information, our understanding of the record that meteorites contain will only ever be partial. The recording of fireball phenomena permits the reconstruction of orbits, as well as determines possible meteorite fall locations to enable the recovery of fresh meteorites whose unique geological record can be fully exploited. This objective has been the driver for a number of dedicated fireball camera network projects dating back to the late 1950s (Ceplecha 1961) and has led to the recovery of multiple meteorites, including two by the Desert Fireball Network (DFN) in Australia during its trial phase (Towner et al. 2011; Spurný et al. 2012).

Over the next few months, the DFN will establish over 50 new Automated Desert Fireball Observatories (ADFOs), with all sky digital cameras, to expand its coverage to an area in excess of 2 million km^2. This will make it the largest fireball network in history, and with >100 TB of data being generated per year, automated systems of data analysis will be needed. The calculation of terminal bright flight mass will form part of the DFN's automated work-flow from fireball detection and triangulation through to dark flight and climate modeling for fall calculations.

Once the light of the fireball goes out, there is usually no way of tracking any remaining fragments to the ground. To model this dark flight, and determine any potential fall positions, the terminal bright flight mass must be ascertained. An automated method of analyzing the bright flight data to extract this information is required and previous methods were investigated for suitability. The two previous approaches to analyzing image data for mass determination are: the photometric method and the dynamic method.

The photometric method relates the luminosity of a fireball to the proportion of kinetic energy that is lost

due to ablation, as a method for obtaining masses (Ceplecha et al. 1998). It uses the luminosity of the fireball to determine the incoming "photometric" mass, and a corresponding luminous efficiency parameter as a proxy for mass loss. To apply this method, a high-resolution light curve of a fireball needs to be acquired. This can be obtained by the addition of a photoelectric photometer to a fireball observatory (Spurný et al. 2012). Not only is this an expensive piece of equipment in itself but also requires additional power supplies, which are limited in the remote locations of the DFN observatories.

Although advancements have been made to the photometric method, including fragmentation as well as dynamical aspects (Ceplecha and ReVelle 2005), it ultimately still requires qualitative comparisons of trajectories with the light curve and manual inputs of fragmentation information (Ceplecha and ReVelle 2005). These qualitative judgments make this method manually intensive and remove the ability to create fully reproducible data.

The dynamic method uses equations of flight through the atmosphere to calculate mass from deceleration (Whipple 1952). In the past, this approach was limited by the accuracy of measurements that could be interpreted from photographic plates (Ceplecha 1961; McCrosky et al. 1971). Ceplecha et al. (1993) used dynamic equations to determine the change in velocity and mass of a meteoroid during its trajectory, along with timings of single fragmentation events. However, the authors were unable to calculate initial masses and therefore relied on initial photometric masses. Considering mass loss is relative, this means the terminal mass is based on this photometric entry mass which may be unreliable (Brykina and Stulov 2012).

Difficulties with the dynamic method are also due to the unknown characteristics of the meteoroid such as density and shape that are required for the dynamic calculation. Work by Stulov et al. (1995) has enabled the application of an analytical solution by combining these unknown parameters into two dimensionless constants. This has been applied by Gritsevich (2008a, 2008b) to the Canadian MORP network data sets, as well as others that have led to meteorite recoveries. This provides good model fits to the data to which it was applied, but assumptions of these same meteoroid characteristics are required to quantify entry mass and subsequently terminal bright flight mass.

Given the limitations of established techniques and improvements to observation technologies, we chose to explore a new approach to the dynamic method. The use of an extended Kalman filter to incorporate the data into the model and provide error estimates was determined to be the most promising approach. An extended Kalman filter is a method of statistically optimizing estimates of an instantaneous state of nonlinear dynamic systems (Grewal and Andrews 1993). An accompanying covariance matrix allows the uncertainties in the state estimations to be determined and propagated. The Kalman filter estimates the bright flight states (distance traveled, mass, and velocity) based on a two-step process of "predict" and "update." However, this method still requires values for meteoroid parameters to be estimated. To maximize confidence in chosen meteoroid parameters, rather than simply picking values, the Extended Kalman Filter is preceded by a dynamic optimization step. This stage is implemented to constrain the combinations of meteoroid characteristics that will permit a fit to the data. These parameters are then used to initialize a series of extended Kalman filters. To test the new method of mass determination, the data set of the Bunburra Rockhole meteorite fall is used as published by Spurný et al. (2012). This is the most complete fireball data set for which a meteorite has been recovered.

The objective of an automated method of mass determination requires an efficient method that will give sufficiently accurate results to determine a practical search area for likely meteorites. As this new approach is based entirely on the photographic data, this significantly reduces the cost of each ADFO unit as there is no requirement for a photoelectric photometer. The new approach to fireball modeling that we outline here will enable the terminal bright flight mass to be approximated from observable data in a fully automatable method, with uncertainties, to enable rapid recovery of meteorite samples which may provide invaluable data for cosmochemists (particularly when combined with orbital data).

MODELING

In the case of the DFN, ADFOs record high-resolution images throughout the night. Fireball observations made by multiple long-exposure cameras can be used to triangulate the position (latitude, longitude, and altitude) of the meteoroid during its flight. To acquire velocity information, however, requires some specialized modifications. Using a customized shutter within the camera lenses, the light path is interrupted at a known frequency (approximately 20 Hz in the ADFO systems). After calibration to remove the effects of lens distortion and triangulation, we have a series of position observations which underpins the subsequent modeling. Velocity may be calculated based on the change in these positions with time. The accuracy of the position observations

determines the accuracy of the velocity values and can cause high scatter in values as seen in the Bunburra Rockhole data set.

All models explored in this work are based on the dynamic equations that characterize the change in mass and velocity of a meteoroid during bright flight through the atmosphere (Baldwin and Sheaffer 1971):

$$\frac{dv}{dt} = -\frac{1}{2}\frac{c_d \rho_a v^2 S}{m} + g \sin \gamma_e \quad (1)$$

$$\frac{dm}{dt} = -\frac{1}{2}\frac{c_h \rho_a v^3 S}{H^*} \quad (2)$$

where m is the meteoroid mass (kg), v is the velocity (m s^{-1}), t is the time (s), c_d is the drag coefficient, ρ_a is the atmospheric density (kg m^{-3}), S is the cross sectional area of the body (m^2), g is the gravitational constant (m s^{-1}), γ_e is the entry angle of the meteoroid to the horizontal, H^* is the enthalpy of sublimation (J kg^{-1}), and c_h is the heat-transfer coefficient.

The position or length along the path of the trajectory, l, is the primary observation extracted from the triangulated images. Its change with time is also included in all models and gives the velocity, i.e., $\frac{dl}{dt} = v$.

A New Approach

The new approach to determining the terminal masses of meteoroids discussed in this paper is a two-step approach, based on the dynamic Equations 1–2. The initial step is a dynamic optimization which runs a global search for the combination of meteoroid characteristics (model parameters) and unknown initial states (initial mass, m_0 and initial velocity, v_0) that provide a good fit to the observational data. The initial position, l_0, is also an initial state but as the length along the flight path is relative, we can set it to be 0 m (similar to Ceplecha and ReVelle 2005). Errors associated with observational uncertainties in this postulation will be taken into account when the extended Kalman filter is initialized.

The second, main step, runs an extended Kalman filter which uses the unknown initial states and parameters from the dynamic optimization to estimate the states (position, l; mass, m; velocity, v) throughout the entire trajectory, including an explicit uncertainty model.

The cross sectional area, S, in the dynamic Equations 1–2, is dependent on the amount of mass lost due to ablation and may be defined as a function of the mass, meteoroid density, ρ_m, and shape parameter, A (a cross sectional area to volume ratio) (equation 3.5; Bronshten 1983)

$$S = A\left(\frac{m}{\rho_m}\right)^{\frac{2}{3}} \quad (3)$$

The change in cross sectional area can be written in terms of the shape change parameter, μ (Equation 4) (Bronshten 1983).

$$S = S_0\left(\frac{m}{m_0}\right)^{\mu} \quad (4)$$

S_0 and m_0 are the initial cross sectional area and initial mass respectively.

By writing Equation 3 in terms of initial parameters only we can combine it with Equation 4 to give

$$S = A_0 \frac{m_0^{2/3-\mu}}{\rho_{m_0}^{2/3}} m^{\mu} \quad (5)$$

Substituting Equation 5 into Equations 1–2 allows the dependent variable S to be removed from the dynamic equations. The modeling of meteoroid states during bright flight will therefore be based on the following differential equations.

$$\frac{dv}{dt} = -\frac{1}{2}\frac{c_d \rho_a A_0}{\rho_{m_0}^{2/3}} m_0^{\left(2/3-\mu\right)} v^2 m^{(\mu-1)} + g \sin \gamma_e \quad (6)$$

$$\frac{dm}{dt} = -\frac{1}{2}\frac{c_h \rho_a A_0}{H^* \rho_{m_0}^{2/3}} m_0^{\left(2/3-\mu\right)} v^3 m^{\mu} \quad (7)$$

Constants Used in All Model Stages

Although the unknown parameters μ and $\frac{c_h}{H^*}$ in Equations 6–7 are variable, they are approximated as constant for both the dynamic optimization and EKF models, along with the remaining unknown initial parameters, m_0, v_0, and $\frac{A_0}{\rho_{m_0}^{2/3}}$ (which will hereby be referred to as the shape-density parameter). This has been the typical assumption in previous works also (Bronshten 1983; Gritsevich 2008b).

The shape change parameter, μ, has a range from 0, being no rotation, to 2/3, indicating that rotation is rapid enough for uniform ablation to occur across the entire surface area. It is typically assumed that μ has a value of 2/3 (Bronshten 1983) and as the dynamic equations are highly sensitive to the value of μ, this

value is also used in our current model and will not be optimized further at this stage. Note that this removes m_0 as a coefficient from Equations 6–7, although m_0 is still present in the optimization as the initial value for mass.

Atmospheric Properties

The NRLMSISE-00 empirical atmosphere model was used to calculate values of atmospheric densities and pressures (Picone et al. 2002). This enables values for temperature, pressure, density, speed of sound, and dynamic viscosity of the atmosphere to be determined as accurately as possible.

Drag Coefficient

The drag coefficient, c_d, can be calculated throughout the trajectory based on a set of fluid dynamic parameters. ReVelle (1976) discusses the dependence of the Reynolds number and flow regime on the drag coefficient, but does not include a criterion for when the Mach regime is no longer hypersonic. This is unlikely to happen during fireball phenomena but is included here for completeness.

The Knudsen number (*Kn*) (Equation 8) can be used to determine the flow regime of the flight path and is the ratio of the mean free path length to the object length. *Kn* may be written as a function of the calculable Mach (*Ma*) and Reynolds (*Re*) numbers (Hayes and Probstein 1959; Truitt 1959) and the ratio of specific heats γ, which for dry air at atmospheric temperatures is taken to be 1.40).

$$Kn = \frac{Ma}{Re} \times \sqrt{\frac{\gamma\pi}{2}} \tag{8}$$

Values of $Kn \geq 10$ indicate free molecular flow, $10 < Kn < 0.1$ a transitional flow regime, and $Kn \leq 0.1$ continuum flow (ReVelle 1976). Within the continuum flow regime, the Mach regime defined by the Mach number needs to be taken into consideration. Only when below a *Ma* of 1.1 is *Re* used to directly calculate the drag coefficient. For values below the critical *Re* associated with drag reattachment ($Re \sim 2e5$) (Schlichting et al. 2000), Equation 11 from Haider and Levenspiel (1989) is used, although it is expected that bright flight values of c_d will remain in the hypersonic regime. Determining the values of c_d for different regimes and turbulence are outlined in Table 1.

For the Bunburra Rockhole data set, the meteoroid remains in the hypersonic regime for the duration of bright flight. In this version of the model, for simplicity, we will assume a hypersonic drag coefficient corresponding to that of a circular cylinder.

Dynamic Optimization

The dynamic optimization based on Equations 6–7 aims to approximate values for $\frac{A_0}{\rho_{m_0}^{2/3}}$ and $\frac{c_h}{H^*}$, as well as an entry mass, m_0, and velocity, v_0. This is performed by assigning assumed values to these parameters within given ranges and the constrained optimization then searches millions of combinations to determine the set of parameters that best fit the position data and return the lowest cost. The cost function used is the sum of the squared errors between the modeled and the observed position data. Costs are normalized to the lowest value, showing 1.0 to be the best fit, to allow comparisons between different parameter sets. As there are multiple unknown parameters, there is a large degree of freedom in the number of plausible combinations. The models that produce cost values >0.98 (best 2%) are selected for consideration in the following stage of the mass determination method.

The parameter constraints used are shown in Table 2. Ranges for ρ_{m_0} are given as assumed preatmospheric meteorite density ranges for typical meteorites. $A_{sphere} = 1.21$ although it is expected that *A* values should typically be in the range of 2–4 (Zhdan et al. 2007). The shape parameter may also be less than that of a sphere depending on which axis is oriented in the direction of the trajectory. The lower and upper bounds for A_0 are chosen as realistic ranges. $\frac{c_h}{H^*}$ is given a wide range so that the average value of this variable throughout bright flight is determined.

Extended Kalman Filter

An extended Kalman filter (EKF) is a method of statistically optimizing estimates of state variables for nonlinear dynamic systems (Grewal and Andrews 1993). For bolide bright flight path analysis, the state vector, x_k, is the instantaneous representation of the state at a time k, and is written in terms of the variables' distance along the bright flight path (l), mass (m), and velocity (v) (Equation 9).

$$x_k = \begin{pmatrix} x_1 \\ x_2 \\ x_3 \end{pmatrix}_k = \begin{pmatrix} l_k \\ m_k \\ v_k \end{pmatrix} \tag{9}$$

The state vector at t_0 is initialized as

$$x_0 = \begin{pmatrix} 0 \\ m_0 \\ v_0 \end{pmatrix} \tag{10}$$

x_k can be determined using the nonlinear state equations:

Table 1. Calculations used to determine the drag coefficient in various fluid dynamic regimes.

Flow regime	Knudsen number range	Mach number range	Drag coefficient formulae
Free molecular flow	$Kn \geq 10$		$c_d = 2.0$ (ReVelle 1976; Masson et al. 1960)
Transition flow regime	$0.1 < Kn < 10$		$c_d = c_d^{cont.} + (c_d^{f.m.} - c_d^{cont.})e^{-0.001Re^2}$ (Khanukaeva 2005)
Continuum flow regime	$Kn \leq 0.1$	$Ma \rightarrow \infty$ *Hypersonic to re-entry*	c_d = 0.92 for spheres (Bronshten 1983; ReVelle 1976; Masson et al. 1960)
			c_d = 4/3 for circular cylinders (Truitt 1959)
			c_d = 2.0 for tiles and bricks (Zhdan et al. 2007)
		$Ma < 8$	$c_d = \frac{24}{Re}[1 + ARe^B] + \frac{C}{1+\frac{D}{Re}}$ where A, B, C, D are variables based on the sphericity of the object (see Haider and Levenspiel 1989)

Table 2. Parameter constraints applied during dynamic optimization.

	Min	Max
m_0	1 kg	1000 kg
v_0	(First velocity value) -3000 m s^{-1}	(First velocity value) $+3000$ m s^{-1}
$\frac{A_0}{\rho_{m_0}^{2/3}}$	$\frac{0.5}{(3500\ \text{kg m}^{-3})^{2/3}}$	$\frac{3.5}{(1500\ \text{kg m}^{-3})^{2/3}}$
$\frac{c_h}{H^*}$	2.5×10^{-7} kg J^{-1}	5.0×10^{-11} kg J^{-1}

$$x_k = f(x_{k-1}, k-1) + w_k \tag{11}$$

where w_k is the process noise with an assumed mean of zero and covariance Q_k (Equation 12).

$$Q_k = E[w_k w_k'] = \begin{bmatrix} \sigma_{l_{prs\ noise}}{}^2 & 0 & 0 \\ 0 & \sigma_{m_{prs\ noise}}{}^2 & 0 \\ 0 & 0 & \sigma_{v_{prs\ noise}}{}^2 \end{bmatrix} \tag{12}$$

An extended Kalman filter is an iterative process that involves two repeated processes. The prediction step for the fireball application will use the dynamic Equations 6–7 along with parameters defined by the previous dynamic optimization to estimate a future state based on all preceding observations. The measurement update step accepts a new observation of the state, in this case the distance along the bright flight path only, and calibrates the predicted outcome using an optimal Kalman gain. This process is schematically illustrated in Fig. 1.

Predicting Future States

The prediction step uses all previous data to derive a suitable state estimate, $\hat{x}_k$:

$$\hat{x}_{k|k-1} = f(\hat{x}_{k-1|k-1}, k) \tag{13}$$

$$P_{k|k-1} = F_k P_{k-1} F_k^T + Q_k \tag{14}$$

F_k is the state transition matrix (Equation 15). P_k is the covariance matrix for the state estimate and is a primary motivation for using an EKF. The diagonal elements can be read to give an indication of the variance for distance, mass, and velocity.

$$F_k = \left[\begin{matrix} \frac{\partial f_1}{\partial l} & \frac{\partial f_1}{\partial m} & \frac{\partial f_1}{\partial v} \\ \frac{\partial f_2}{\partial l} & \frac{\partial f_2}{\partial m} & \frac{\partial f_2}{\partial v} \\ \frac{\partial f_3}{\partial l} & \frac{\partial f_3}{\partial m} & \frac{\partial f_3}{\partial v} \end{matrix} \right] \Bigg|_{x=x_k} \tag{15}$$

where:

$$l_{k+1} = f_1(l_k, m_k, v_k, t_k) = l_k + \frac{\mathrm{d}l_k}{\mathrm{d}t_k}\Delta t = l_k + v_k \Delta t \tag{16}$$

$$\begin{aligned} m_{k+1} &= f_2(l_k, m_k, v_k, t_k) = m_k + \frac{\mathrm{d}m_k}{\mathrm{d}t_k}\Delta t \\ &= m_k - (k_m v_k^2 m_k^{\mu})\Delta t \end{aligned} \tag{17}$$

$$\begin{aligned} v_{k+1} &= f_3(l_k, m_k, v_k, t_k) = v_k + \frac{\mathrm{d}v_k}{\mathrm{d}t_k}\Delta t \\ &= v_k - (k_v v_k^2 m_k^{(\mu-1)} - g\sin\gamma_e)\Delta t \end{aligned} \tag{18}$$

And:

$$k_v = \frac{1}{2}\frac{c_d \rho_a A_0}{\rho_{m_0}{}^{2/3}} m_0^{\left(2/3-\mu\right)}, k_m = \frac{1}{2}\frac{c_h \rho_a A_0}{H^* \rho_{m_0}{}^{2/3}} m_0^{\left(2/3-\mu\right)}. \tag{19}$$

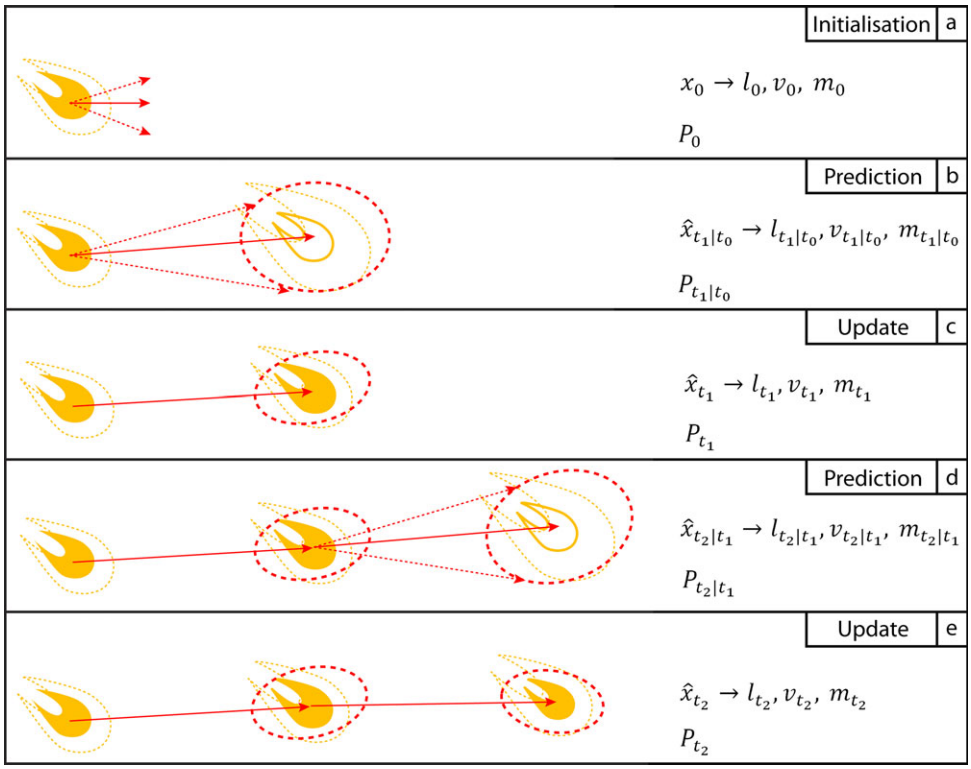

Fig. 1. Illustration of the extended Kalman filter process. a) Initialization of state. The P_0 matrix defines the initial uncertainties (dashed) in velocity (red arrow) and mass (yellow). b) A prediction is made and the state matrix, $\hat{x}_{k|k-1}$, has covariances defined by $P_{k|k-1}$. Mass uncertainties are initially large, as is position (dashed red). (c) Measurement update calibrates the state and uncertainties decrease (d) prediction step (e) measurement step. These two processes (d–e) repeat to give a final state estimate ($\hat{x}_f$) and associated covariance matrix (P_f).

Measurement Updates

The measurement update step follows an observation z_k (Equation 20), which for ADFO observations is only the distance data $l_k = (x_1)_k$. H_k provides a relationship between the state of the dynamic system and the measureable observations, simply put, $H_k x_k = l_k$. n_k is the measurement noise with a mean of zero and covariance R_k (Equation 21). R_k, therefore, accounts for errors between measured position and true position due to aspects such as camera calibration, triangulation, camera resolution etc.

$$z_k = H_k x_k + n_k \tag{20}$$

$$R_k = E[n_k n_k'] = \left[{\sigma_{z_k}}^2\right] \tag{21}$$

The predicted measurement can be made using the output of Equation 13

$$\hat{z}_k = H_k \hat{x}_{k|k-1} \tag{22}$$

The residual difference between z_k and $\hat{z}_k$ is y_k (Equation 23). S_k (Equation 24) projects the system uncertainty into the measurement space and includes uncertainties in the model up to t_{k-1}, as well as the noise covariance of the current measurement. The optimum Kalman gain, K_k (Equation 25) is used to update the state ($\hat{x}_k$) and covariance matrices (P_k) (Equations 26–27)

$$y_k = z_k - \hat{z}_k \tag{23}$$

$$S_k = H_k P_{k|k-1} H_k^T + R_k \tag{24}$$

$$K_k = P_{k|k-1} H_k^T S_k^{-1} \tag{25}$$

$$\hat{x}_k = \hat{x}_{k|k-1} + K_k y_k \tag{26}$$

$$P_k = (I - K_k H_k) P_{k|k-1} \tag{27}$$

The square root of the diagonal elements of P_k is plotted as error bars so that the evolution of state uncertainty with time can be visualized in a meaningful way.

Fireball Applications

For the nonlinear bolide dynamical equations, $\hat{x}_{k+1|k}$ is calculated by solving the nonlinear

Equations 6–7 between t_{k+1} and t_k. P_k, however, is solved using the linearized state transition matrix, F_k (Equation 28). The linearization of F_k approximates to:

$$F_k = \begin{pmatrix} 1 & 0 & \Delta t \\ 0 & 1 - k_m v_0^3 m_0^{\mu}\left(\frac{\mu}{m_0}\right)\Delta t & -k_m v_0^3 m_0^{\mu}\left(\frac{3}{v_0}\right)\Delta t \\ 0 & -k_v v_0^2 m_0^{(\mu-1)}\left(\frac{(\mu-1)}{m_0}\right)\Delta t & 1 - k_v v_0^2 m_0^{(\mu-1)}\left(\frac{2}{v_0}\right)\Delta t \end{pmatrix} \quad (28)$$

The errors associated with this linearization are included in the process covariance matrix, Q_k, along with the uncertainties in the model due to unmodeled factors such atmospheric disturbances and uncertainties in the atmospheric model used. The value of Q_k encapsulates these model uncertainties and is specific to the individual data set being analyzed.

P_0 is initialized at t_0 as a function of initial data uncertainty (Equation 29). As the length along the flight path is relative to the initial point, there is no model error in σ_{l_0} being zero (error in *observation* of positions is accounted for in R_k). The initial mass covariance is given as 0.5 times the initial mass determined by the dynamical optimization. Distance error and timing information give uncertainties of up to ± 1500 m s^{-1} for velocity.

$$P_0 = \begin{bmatrix} \sigma_{l_0}^2 & 0 & 0 \\ 0 & \sigma_{m_0}^2 & 0 \\ 0 & 0 & \sigma_{v_0}^2 \end{bmatrix} = \begin{bmatrix} 0 & 0 & 0 \\ 0 & \left(m_0 \times 0.5\,\mathrm{kg}\right)^2 & 0 \\ 0 & 0 & \left(1500\,\mathrm{km\,s^{-1}}\right)^2 \end{bmatrix} \quad (29)$$

The initial errors are large but P_k is updated throughout the iterative estimation, giving a concrete representation of the evolution of the confidence of the state estimate, incorporating the uncertainties defined by the process noise covariance, Q_k (Equation 12), and the measurement noise covariance, R_k (Equation 21). The measurement noise covariance for the bolide problem is set to be $(100\ \mathrm{m})^2$ and is dependent on camera resolution, the angle of the fireball with respect to the camera, and calibration of lens distortion.

Smoothing Problem

More generally, we can apply a smoothing estimator to our fireball data sets, as we will always have the observations from the entire trajectory available when the estimation is performed. A *filtering* estimator, such as described above, uses only past data (and hence is suitable for real-time estimation), whereas a *smoothing* estimator uses all data (future and past) to generate an optimal state estimate. The Rauch–Tung–Striebel (RTS) smoothing algorithm is implemented using the method described by Sarkka (2008). The resulting state estimate values for the trajectory are improved, along with their uncertainties.

RESULTS

The most complete data set available to test this method is that of Bunburra Rockhole, published by Spurný et al. (2012), which contains 113 data points with time, length of segment, and altitude information. As this data resulted in a recovered meteorite, constraints are available on final mass (Spurný et al. 2012), and cosmic ray exposure rates (Welten et al. 2012) provide an estimate of initial body diameter.

Dynamic Optimization

The dynamic optimization method described earlier, is applied to the data set using the constraints on parameters given in Table 2. Five parameter sets produce a fit with cost values >0.98 (Table 3). The initial masses range from 27.65 to 30.12 kg (Fig. 2) but the final masses converge to values of ~2.4 kg.

Figure 2 allows a visual comparison of these model outputs to the raw data. The parameter sets defined in Table 3 are used to initialize a set of Kalman filters that will take the data itself into consideration to determine a final mass.

Kalman Filter

The Extended Kalman Filter runs separately on each set of parameters resulting from the dynamical optimization stage. The final states of each model setup are given in Table 4.

The change in state values during the iterative EKF process are graphed against time with covariance plotted as approximate error bars (Fig. 3). The uncertainties are high initially. Mass uncertainties are only constrained by the data through the link to velocity with the dynamic equations and therefore remain high while the iterative process determines a value.

After running the forward EKF, the Rauch–Tung–Striebel smoothing algorithm is run (Fig. 4). The outcome of smoothing produces an initial entry mass of 30.20 ± 6.53 kg.

Checking Results Using the Dimensionless Coefficient Method

As a comparison, we also analyzed the Bunburra Rockhole data set using the approach based on Stulov et al. (1995) and applied by Gritsevich (2008b). In this

Table 3. Top five best fit parameter sets resulting from dynamical optimization.

Normalized sum of square differences to position	m_0 (kg)	v_0 (m s^{-1})	$\frac{A_0}{\rho_{m_0}{}^{2/3}}$ (kg m^{-3})$^{-2/3}$	$\frac{c_h}{H^*}$ ($\times 10^{-8}$ J kg^{-1})	l_f (m)	m_f (kg)	v_f (m s^{-1})
1.00000	30.12	13198	0.009511	4.82	60071.8	2.36	6109
0.99859	30.95	13203	0.009689	4.76	60042.4	2.50	6100
0.98862	29.82	13203	0.009545	4.68	60061.8	2.51	6124
0.98544	28.64	13204	0.009466	4.66	60057.6	2.44	6125
0.98108	27.65	13205	0.009394	4.64	60052.7	2.38	6126

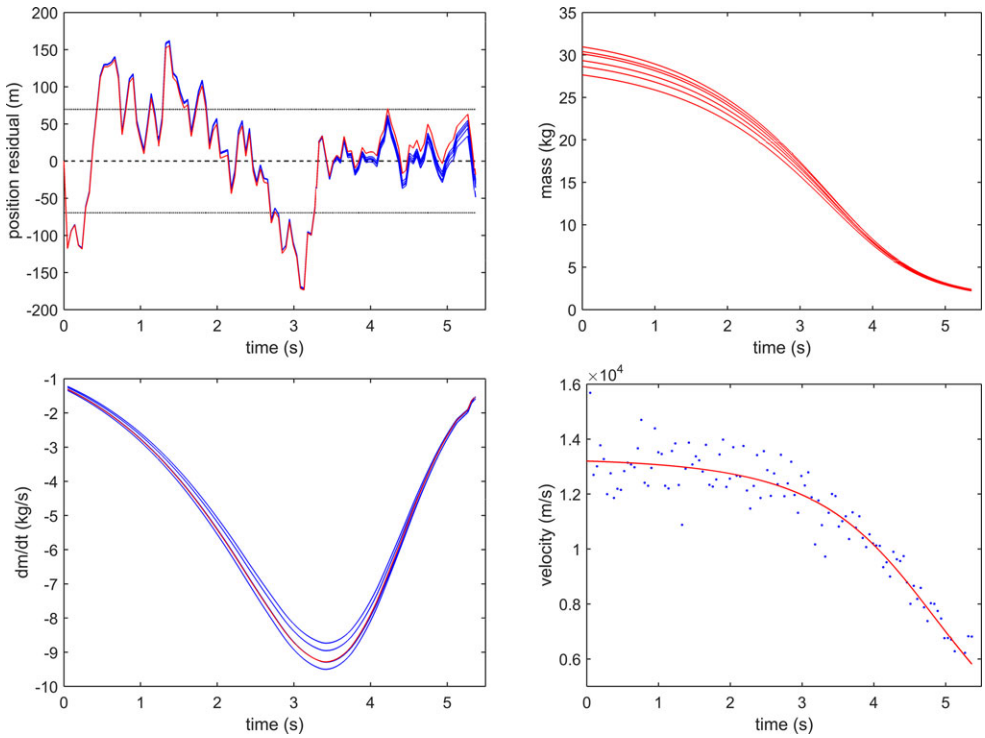

Fig. 2. Top left: position data subtracted from modeled position for models with parameters given in Table 3. Red curve is model that gives the lowest normalized sum of square differences (initial mass of 30.12). Dotted line is one standard deviation (70.14 m). Top right: shows associated change in mass for corresponding model parameters with costs >0.98. Bottom left: derivative of mass with time for models. Bottom right: comparison of models (red curves) to calculated velocity (blue points).

Table 4. Final states (x_f, m_f, v_f) for parameter sets from dynamic optimization corresponding to the following initial masses.

m_0 (kg)	x_f (m)	m_f (kg)	v_f (m s^{-1})
30.12	60032 ± 62	2.30 ± 1.63	6052 ± 241
30.95	60032 ± 62	2.47 ± 1.67	6057 ± 236
29.82	60033 ± 62	2.40 ± 1.67	6061 ± 238
28.64	60033 ± 62	2.35 ± 1.66	6062 ± 240
27.65	60033 ± 62	2.29 ± 1.64	6062 ± 242

method, the dynamic Equations 1–2 are modified by normalizing the values of mass, velocity, and altitude (h) to the entry mass, entry velocity, and the scale height of the homogeneous atmosphere (h_0 = 7160 m), respectively. A set of dimensionless parameters (ballistic coefficient, α [26], and mass loss parameter, β [31]) are substituted to remove the need of unknown individual variables.

$$\alpha = \frac{c_d \rho_0 h_0 A_0 {m_0}^{-1/3}}{2{\rho_{m_0}}^{2/3} \sin\gamma} \tag{30}$$

$$\beta = (1-\mu)\frac{c_h v_0^2}{2c_d H^*} \tag{31}$$

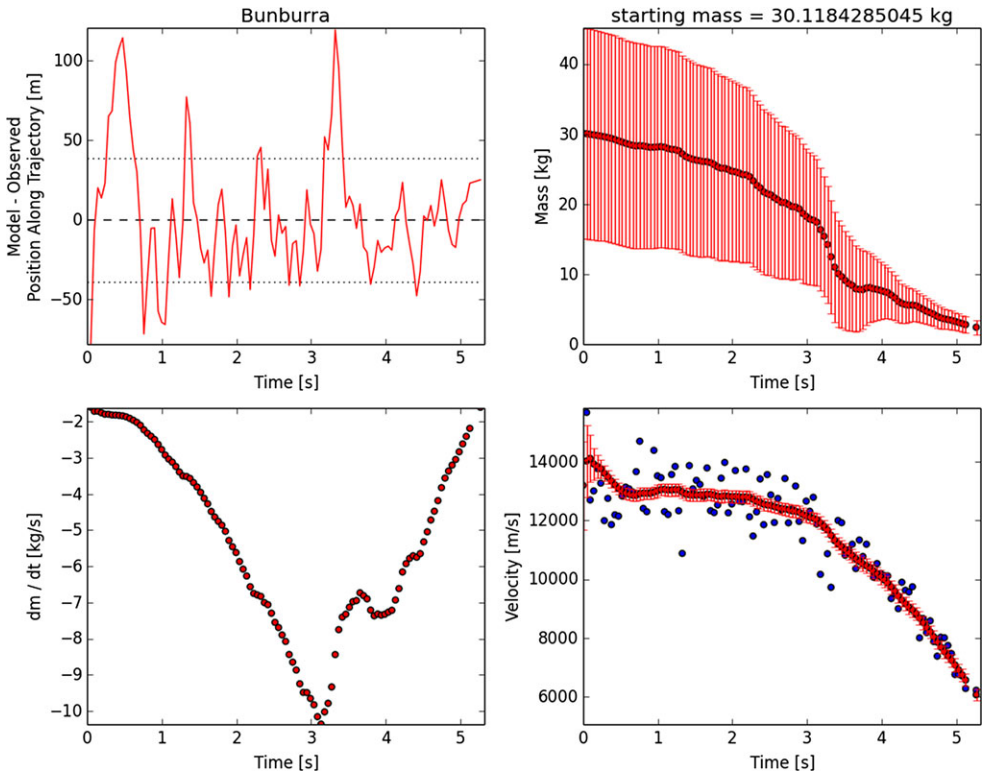

Fig. 3. Extended Kalman Filter results for initial mass of 30.12 kg. Top left: residual plot of position data subtracted from EKF position estimate. Dotted lines represent one standard deviation (38.83 m). Top right: mass error bars are extracted from the constantly updating P matrix. Bottom left: derivative of mass with time, showing relative mass loss predicted for each time step. Bottom right: blue points represent calculated velocity values. Red points are EKF estimates of velocity given only past data from each time step. Although mass and velocity will never realistically increase, as the EKF is provided with new data at each time step, it corrects the values of previous estimates.

where ρ_0 is the atmospheric density near the surface and γ is the trajectory entry angle.

The Q_4 method of least-squares minimization defined by Gritsevich (2008b) is used to create a fit of the Kulakov and Stulov (1992) Equation 32 to the Bunburra Rockhole data set.

$$y = \ln \alpha - \ln(-\ln V) + 0.83\beta(1 - V) \qquad (32)$$

where $y = \frac{h}{h_0}$ and $V = \frac{v}{v_0}$.

The isothermal atmosphere approximation is used to derive Equation 32: $\rho_a = e^{-y}$, making it difficult to implement a more accurate atmosphere model.

Although this method has proved successful on previous fireball data sets (Gritsevich 2008a), these are limited to fewer than 20 velocity points with an average based smoothing applied (Ceplecha 1961). The value of v_0 that is used to normalize all velocity values is simply the initial velocity. For the Bunburra Rockhole data set, the 113 data points show high scatter and the velocity range within the first half a second has a range of over 3500 m s^{-1}. It was found that the noise in the raw data could not be accommodated by this method without pretreating the data, making it rather unsuitable for use in an automated data pipeline where large noisy data sets need to be processed.

Smoothing the data using a five-point moving average, and using the average initial velocity from Table 3, 13,200 m s^{-1}, and a value of 2/3 for the shape change parameter allows a result to be calculated as a comparison to the new method. This gives $\alpha = 25.23$ and $\beta = 1.53$ (Fig. 5). The equation for the ballistic coefficient (Equation 30) allows an initial mass to be calculated. By assuming values of the shape-density parameter from the dynamic optimization, and a constant drag coefficient of 1.3, an approximate value for m_0 is determined to be 84.92 kg.

When used in the following Equation 33, along with a value of 2/3 for rotation, a final mass of 1.90 kg results.

$$m_f = m_0 e^{\left(-\beta \frac{1 - V_f^2}{1 - \mu}\right)} \qquad (33)$$

(equation 6 [Gritsevich 2008b])

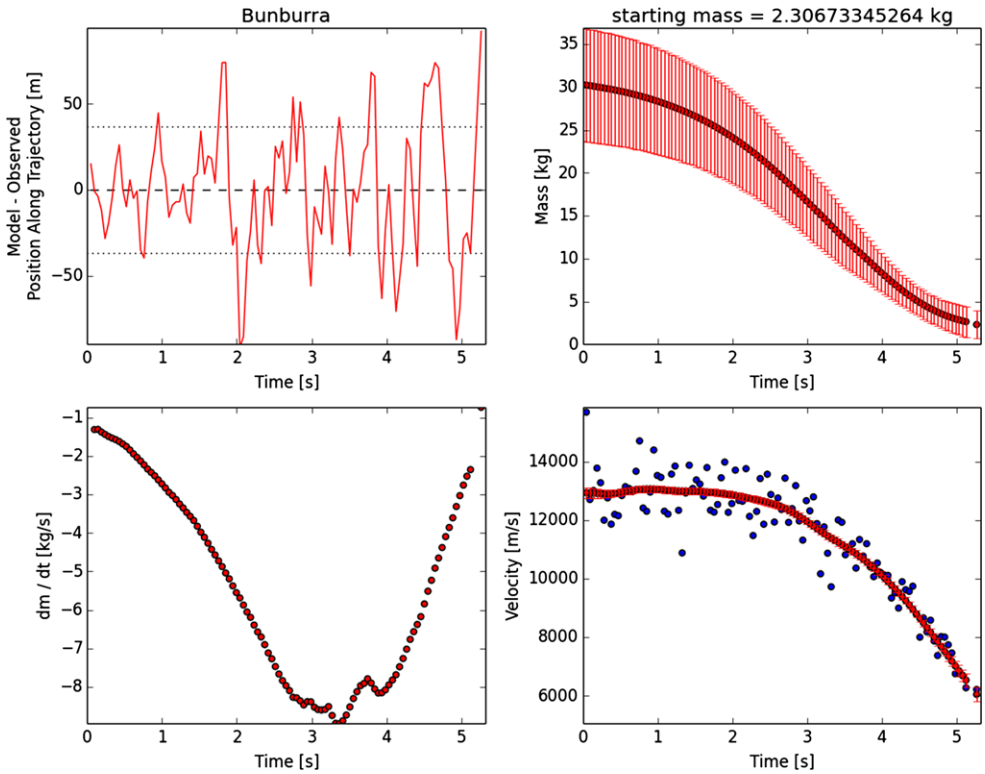

Fig. 4. RTS smoothing filter results for the best fit parameter set. Top left: residual plot of position data subtracted from RTS position estimate. Dotted lines represent one standard deviation (36.73 m). Top right: predicted mass along trajectory. Bottom left: derivative of mass with time, showing relative mass loss predicted for each time step. Bottom right: blue points represent calculated velocity values. Red points are RTS estimates of velocity given both past and future state estimates.

It is difficult to assess the error in this case, and the ranges in initial and final masses are harder to obtain. The amount of scatter in the velocity data is significant and a change in initial velocity used by 1% can result in initial masses varying by ±30 kg and final masses to be ±2 kg.

DISCUSSION

Determining Model Parameters

The dynamical optimization of the Bunburra Rockhole data set returned a large number of parameter sets with cost values >0.9, although only five with >0.98, all of which show relatively similar starting masses. The ranged (27.65–31.12 kg) initial masses converge (Fig. 2) to give very similar final mass values (Table 3). As the final masses are needed for determining any potential fall positions, it is more important that these values be limited. It should be remembered that the dynamic optimization is estimating appropriate meteoroid parameters to use as inputs in our main model (EKF step) based on this specific fireball data set. Previous works have assumed "typical," or average meteoroid parameter values, without the link to the data from the event in question (e.g., densities by Borovička et al. [1998, 2013] and McCrosky et al. [1971]; shape density coefficient used by Ceplecha and ReVelle [2005] and Spurný et al. [2012]). We believe that this is an advantage of our approach. This step gives us greater confidence in the estimates to be used in the EKF step, especially considering the similarities in meteoroid characteristics of the top results (Table 3).

The shape parameter and preatmospheric meteoroid density cannot be uniquely identified in this model. The values of $\frac{A_0}{\rho_{m_0}{}^{2/3}}$ in Table 3 could correspond to a spherical object ($A_0 = 1.21$) with a preatmospheric meteoroid density of ~1400 kg m^{-3}, a circular cylinder with a cross sectional diameter to length ratio of roughly 1:1 and ρ_{m_0} ~2700 kg m^{-3}, or even a 3:2:1 triaxial ellipsoid (as suggested by Zhdan et al. 2007) with ρ_{m_0} ~3500 kg m^{-3}. A unique solution is not needed for finding any potential meteorites and any fragments found will be able to resolve these two parameters.

Knowing the Bunburra Rockhole bulk meteorite density to be 2700 kg m^{-3} (Spurný et al. 2012) enables us to approximate the meteoroid shape, A ~1.85. This corresponds to a circular cylinder with a cross sectional

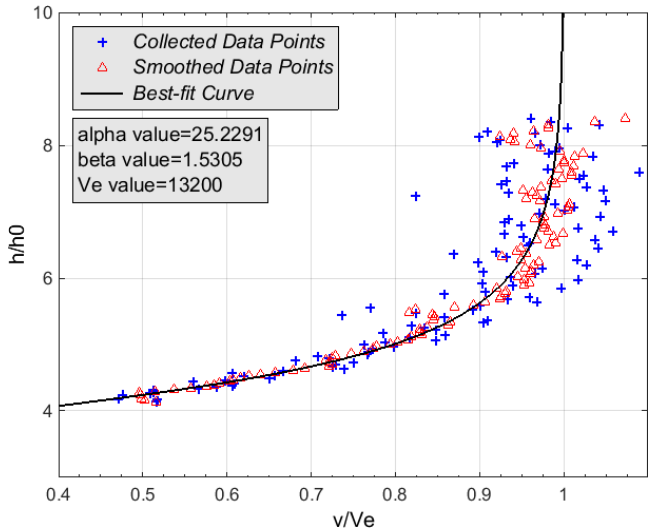

Fig. 5. Raw (+) and smoothed (Δ) Bunburra Rockhole velocities normalized to an entry velocity of 13,200 m s^{-1} versus normalized altitude, y. Best fit for Equation 32 is shown which is produced using $\alpha = 25.23$ and $\beta = 1.53$.

Table 5. Values of $\frac{c_h}{H^*}$ determined by the dynamical optimization stage (Table 3) and the subsequent approximate values of c_h. σ values are given for a drag coefficient of 1.3.

$\frac{c_h}{H^*}$ ($\times 10^{-8}$ J kg^{-1})	c_h given H* = 2 × 10^6 J kg^{-1}	σ ($\times 10^{-6}$ s^2 m^{-2})
4.820	0.0964	0.0371
4.755	0.0951	0.0366
4.684	0.0937	0.0360
4.662	0.0932	0.0359
4.644	0.0929	0.0357

diameter to length ratio of roughly 1:1, or a 3:2:1.5 axial ellipsoid. If the value of A and ρ_m were to remain constant, these values of A_0 and ρ_{m_0} with the given initial mass corresponds approximately to a cross sectional area of 0.092 m^2. Figure 7.2 in Stulov et al. (1995) shows a distribution of values of H^* for bolides, resulting in an overwhelming majority with entry masses >1 kg, having values close to 2 × 10^6 J kg^{-1}. If this value is assumed for H^*, values for c_h can be approximated (Table 5). It may be useful as a comparison to give also the ablation coefficient, $\sigma = \frac{c_h}{c_d H^*}$ (Table 5), given a drag coefficient of 1.3. σ values are very similar to the apparent ablation coefficient values determined by Spurný et al. (2012). This is to be expected as fragmentation is currently not incorporated to allow intrinsic values of σ to be determined by the dynamic optimization.

The Model Solution

The initial 3 s of the Bunburra Rockhole velocity data is rather noisy, varying by around ±2000 m s^{-1}. However, it is handled coherently by our EKF approach without the inclusion of an arbitrary smoothing step. The EKF optimizes the state of the bolide at each individual time-step. Each point on the graphs of Fig. 3 are the instantaneous representation of the state at a given time given only the past data. The values are variable within their error ranges as the data are not perfect. It is not a simple least squares, it does not aim to reduce the covariance, rather it "learns" from the data and predicts where it should be and carries the errors forward. The covariance incorporates both measurement uncertainty and scatter to give a comprehensive understanding of the errors associated with each state. Where previous works have used best fit modeling, primarily least squares fits (Ceplecha and ReVelle 2005), by taking this intelligent "predict" and "update" approach, the EKF method is likely to come closer to approximating the real position of the object at any given time. This is reflected in the lower standard deviation of the residual plots (38.83 m for EKF versus 70.14 m for dynamical optimization)

Despite the variation in parameter sets provided by the dynamical optimization, the final masses which are most important for finding any potential fall positions (and therefore the primary solution of this modeling), are very similar and their range constrains the final bright flight mass. The best estimate of final mass is 2.30 ± 1.63 kg and is close to the published value of 1.1 kg by Spurný et al. (2012).

The initial mass determined by Spurný et al. (2012) using both the methods described by both Ceplecha et al. (1998) and Ceplecha and ReVelle (2005) is 22.0 ± 1.3 kg. Cosmic ray exposure rates were analyzed for the Bunburra Rockhole meteorite; however, the pre-entry radius was determined to be larger than a radius corresponding to a mass of 22 kg (Welten et al. 2012). By performing a reverse extended Kalman filter, the entry mass is determined to be closer to 30.20 ± 6.53 kg. This corresponds to a pre-entry radius of around 17.1 cm. This is close to the 13–17 cm range determined by (Welten et al. 2012).

Although fragmentation is not yet explicitly handled using this method, the data reflects both effects of ablation and fragmentation. The process noise Q_k in the EKF model handles some degree of unexpected mass change, allowing these variations to be incorporated in the final mass estimates.

Furthermore, sudden increases in the magnitude of the state variance matrix P_k can give an indication that a fragmentation event may have occurred, along with

examining the change in mass with time (Figs. 3 and 4). It is noticeable from both Figs. 3 and 4 that there are peaks of maximum mass loss at around 3.133 and 3.845 s as well as at 4.415 s in Fig. 3. It is likely that these correspond to fragmentation events. These times correspond to altitudes of 41.31, 37.16, and 34.18 km, respectively, allowing a comparison to fig. 13 in Spurný et al. (2012) which shows significant changes of mass at 37.8 and 35.85 km altitude. The significant mass loss event seen in fig. 13 in Spurný et al. (2012) at 54.9 km (corresponding to 1.0 s) is not evident, although it is well within the large error bracket given at this time. Future work will aim to capture this fragmentation information in a coherent and consistent way.

The scatter in the Bunburra Rockhole data set presented difficulties when initially attempting to use the method outlined by Gritsevich (2008a). After smoothing the data and using the initial parameters determined by the dynamic optimization, final values are similar to those determined using this new method. The dependence on an initial velocity for normalization makes it very sensitive to initial scatter and there is no constraint on the errors this or the smoothing may cause. The EKF method avoids these dependences.

CONCLUSION

The method outlined here provides a consistent and detailed approach to characterizing meteoroids without the need for brightness data as they pass through the atmosphere. In addition, it provides a rigorous way of propagating uncertainties in trajectory states (position, mass, and velocity), something that previous approaches have not explicitly described.

A dynamic optimization determines the optimum parameters for the meteoroid flight such as the shape-density parameter and initial mass. An extended Kalman filter then includes observation and dynamic uncertainty models, which are valuable in understanding the errors in the model states, and which can adapt to fragmentation events or other unexpected dynamic changes. The initial (30.20 ± 6.53 kg) and final masses (2.30 ± 1.63 kg) calculated for the Bunburra Rockhole data set is within the range of previously published values by Spurný et al. (2012) (22.0 ± 1.3 and 1.1 kg, respectively) and corresponds with cosmic ray exposure studies (Welten et al. 2012) to constrain preatmospheric radius and mass. Although the method used by Gritsevich (2008b) was re-created using the meteoroid characteristics determined by dynamic optimization, the sensitivity of this method to (widely varying) data for initial entry velocity translates to a range of estimates for entry and terminal masses. As the errors are not quantified, the confidence in mass calculations using this method—crucial for automating our data flow and constraining search areas—cannot be constrained.

The two-step approach outlined in this paper is an automated method which will allow the DFN to reduce data for every observed fireball, rather than only selecting high value or unusual cases. For the subset that involve a meteorite fall, this approach will calculate multiple fall positions with comprehensive error values to allow for efficient recovery searches. Work still needs to be carried out on integrating the variability in the heat-transfer coefficient. The assumption in this method that it remains constant throughout the trajectory is a simplification. The identification and analysis of fragmentation events also needs to be incorporated in a more coherent and consistent manner.

Acknowledgments—This work was funded by the Australian Research Council as part of the Australian Laureate Fellowship scheme. The authors thank N. Artemieva, J. Borovička, and O. Popova for constructive comments and reviews that significantly improved the quality of the final manuscript.

Editorial Handling—Dr. Natalia Artemieva

REFERENCES

Baldwin B. and Sheaffer Y. 1971. Ablation and breakup of large meteoroids during atmospheric entry. *Journal of Geophysical Research* 76:4653–4668.

Borovička J., Popova O., Nemtchinov I., Spurný P., and Ceplecha Z. 1998. Bolides produced by impacts of large meteoroids into the Earth's atmosphere: Comparison of theory with observations. I. Benesov bolide dynamics and fragmentation. *Astronomy & Astrophysics* 334:713–728.

Borovička J., Tóth J., Igaz A., Spurný P., Kalenda P., Haloda J., Svoreň J., Kornoš L., Silber E., Brown P., and Husárik M. 2013. The Košice meteorite fall: Atmospheric trajectory, fragmentation, and orbit. *Meteoritics & Planetary Science* 48:1757–1779.

Bronshten V. A. 1983. *Physics of meteoric phenomena. Fizika meteornykh iavlenii, Moscow, Izdatel'stvo Nauka, 1981.* Dordrecht: D. Reidel Publishing Co. 372 p.

Brykina I. and Stulov V. 2012. The reciprocal role of convective and radiant heat exchange in the meteor-parameter range. *Doklady Physics* 57:164–165.

Ceplecha Z. 1961. Multiple fall of Příbram meteorites photographed. 1. Double-station photographs of the fireball and their relations to the found meteorites. *Bulletin of the Astronomical Institutes of Czechoslovakia* 12:21.

Ceplecha Z. and ReVelle D. O. 2005. Fragmentation model of meteoroid motion, mass loss, and radiation in the atmosphere. *Meteoritics & Planetary Science* 40:35–54.

Ceplecha Z., Spurny P., Borovička J., and Keclikova J. 1993. Atmospheric fragmentation of meteoriods. *Astronomy & Astrophysics* 279:615–626.

Ceplecha Z., Borovička J., Elford W. G., ReVelle D. O., Hawkes R. L., Porubčan V., and Šimek M. 1998. Meteor phenomena and bodies. *Space Science Reviews* 84:327–471.

Grewal M. and Andrews A. P. 1993. *Kalman filtering: Theory and practice*. Upper Saddle River, NJ: Pearson Prentice Hall.

Gritsevich M. 2008a. The Příbram, Lost City, Innisfree, and Neuschwanstein falls: An analysis of the atmospheric trajectories. *Solar System Research* 42:372–390.

Gritsevich M. 2008b. Validity of the photometric formula for estimating the mass of a fireball projectile. *Doklady Physics* 53:97–102.

Haider A. and Levenspiel O. 1989. Drag coefficient and terminal velocity of spherical and nonspherical particles. *Powder Technology* 58:63–70.

Hayes W. D. and Probstein R. F. 1959. *Hypersonic flow theory*. New York: Academic Press.

Khanukaeva D. Y. 2005. Calculation of variable drag and heat-transfer coefficients in meteoritic physics equations. In *Modern meteor science: An interdisciplinary view*, edited by Hawkes R. L., Mann I., and Brown P. G. Dordrecht, the Netherlands: Springer. pp. 433–439.

Kulakov A. and Stulov V. 1992. Determination of meteor body parameters from observational data. *Astronomicheskii Vestnik* 26:67–75.

Masson D. J., Morris D. N., and Bloxsom D. E. 1960. *Measurements of sphere drag from hypersonic continuum to free-molecule flow*. Santa Monica, California: RAND Corporation.

McCrosky R., Posen A., Schwartz G., and Shao C.-Y. 1971. Lost City meteorite—Its recovery and a comparison with other fireballs. *Journal of Geophysical Research* 76:4090–4108.

Picone J., Hedin A., Drob D. P., and Aikin A. 2002. NRLMSISE-00 empirical model of the atmosphere: Statistical comparisons and scientific issues. *Journal of Geophysical Research: Space Physics (1978–2012)* 107:1468.

ReVelle D. O. 1976. *Dynamics and thermodynamics of large meteor entry: A quasi-simple ablation model*. Ottawa, Canada: Herzberg Institute of Astrophysics, National Research Council Canada.

Sarkka S. 2008. Unscented Rauch-Tung-Striebel Smoother. *Automatic Control, IEEE Transactions on* 53:845–849.

Schlichting H., Gersten K., and Gersten K. 2000. *Boundary-layer theory*. New York: Springer.

Spurný P., Bland P. A., Borovicka J., Shrbený L., McClafferty T., Singelton A., Bevan A. W. R., Vaughan D., Towner M. C., and Deacon G. 2012. The Bunburra Rockhole meteorite fall in SW Australia: Fireball trajectory, luminosity, dynamics, orbit, and impact position from photographic and photoelectric records. *Meteoritics & Planetary Science* 47:163–185.

Stulov V., Mirskii V., and Vislyi A. 1995. *Aerodynamics of bolides*. Moscow: Science. Fizmatlit.

Towner M., Towner M. C., Bland P. A., Spurný P., Benedix G. K., Dyl K., Greenwood R. C., Gibson J., Franchi I. A., Shrbený L., Bevan A. W. R., and Vaughan D. 2011. Mason Gully: The second meteorite recovered by the Desert Fireball Network. *Meteoritics & Planetary Science Supplement* 74:5124.

Truitt R. W. 1959. *Hypersonic aerodynamics*. New York: Ronald Press Co.

Welten K. C., Meier M. M., Caffee M. W., Laubenstein M., Nishizumi K., Wieler R., Bland P. A., Towner M. C., and Spurný P. 2012. Cosmic-ray exposure age and preatmospheric size of the Bunburra Rockhole achondrite. *Meteoritics & Planetary Science* 47:186–196.

Whipple F. L. 1952. Meteoritic phenomena and meteorites. *Physics and Medicine of the Upper Atmosphere* 137:149–153.

Zhdan I., Stulov V., Stulov P., and Turchak L. 2007. Drag coefficients for bodies of meteorite-like shapes. *Solar System Research* 41:505–508.